ELSEVIER

Contents lists available at ScienceDirect

International Journal of Heat and Mass Transfer

journal homepage: www.elsevier.com/locate/ijhmt





Study of bubble dynamics detaching from flexible channels

Xiaojing Ma^{a,b,*}, Songhe Wang^a, ShiXin Nong^a, Chunjiao Han^a, Jinliang Xu^{a,b}, Khellil Sefiane^c

- a Beijing Key Laboratory of Multiphase Flow and Heat Transfer for Low Grade Energy Utilization, North China Electric Power University, Beijing 102206, PR China
- b Key Laboratory of Power Station Energy Transfer Conversion and System of Ministry of Education, North China Electric Power University, Beijing 102206, PR China
- c School of Engineering, University of Edinburgh, King's Buildings, Mayfield Road, Edinburgh EH93JL, Scotland, United Kingdom

ARTICLE INFO

Keywords:
Boiling heat transfer
Elastic fins
Bubble dynamics
Confined space

ABSTRACT

Exploring bubbles dynamics generated on flexible substrates in confined spaces is essential to achieve the potential of this configuration for two-phase flow in various engineering applications. Especially, bubble dynamics could significantly impact the heat transfer performance. This study numerically examines bubble dynamics between flexible plates with different elastic moduli to promote bubble departure. The departure time and velocity of bubbles during their motion through flexible channels are investigated and validated by experiments. An optimal elastic modulus which minimizes bubble departure time is identified. It is found that bubble dynamics with elastic plates exhibit shorter bubble departure time due to the energy conversion between kinetic energy and elastic potential energy. The plate morphology and the contact length between the bubble and elastic plates are also found to significantly affect bubble dynamics. Deformations in the plates, such as necked-in or necked-out shapes, are observed only in cases where the elastic modulus is to $E \le 10^7$ Pa due to elastic capillary effect. A necked-out morphology helps store elastic potential energy, facilitating bubble departure. This study provides a theoretical basis and design principles for applying flexible materials in microfluidic systems.

1. Introduction

Manipulation of bubble dynamics is vital in the development of various industrial applications [1–3]. High bubble removal rate from the electrode can enhance electrolysis efficiency and improve system stability in electrochemical technology [4]. In the field of medicine, precise control of bubble movement enhances the therapeutic effect and ensures patient safety [5]. In heat and mass transfer, the key mechanisms of boiling heat transfer include micro-layer evaporation at bubble bases [6], turbulent mixing and wall rewetting caused by bubble departure [7, 8]. Improving bubble growth could improve micro-layer evaporation, while promoting bubble departure enhanced mixing and rewetting [9]. Bubbles are often disordered in practical applications. Effective ways for removing bubbles are a hot topic nowadays. Poor bubble dynamics in confined space could cause a series of operational challenges and inefficiencies. The nucleation and departure of bubbles significantly influenced bubble dynamics in confined spaces. The sites of bubble nucleation determine the initial growth environment; unfavorable sites can extend the bubble cycle and hinder departure. Excessively high nucleation density leads to frequent bubble coalescence, resulting in

larger bubbles [10]. Both extended cycles and increased bubble sizes might cause blockage [11]. Bubble departure size is a factor affecting bubble dynamics in a confined space, determined by the forces acting on bubbles. These forces are divided into driving forces induced by buoyancy and resistance forces induced by surface tension. Enhancing the former or reducing the latter could effectively decrease the bubble diameter and improve bubble dynamics. Contact angle determines the theoretical value of surface tension. However, it is necessary to note that a pinning force would be generated due to contact angle hysteresis [12]. Additionally, the evaporation momentum force could be used to modulate bubble departure direction, which could benefit bubble departure from the channel [13,14].

Numerous researchers conducted extensive studies on the issue of poor bubble dynamics in confined space [15–17]. Pan et al[18] demonstrated that when bubble blockage occurred within the channel, the liquid refluxed back into the channel, leading to a reflux phenomenon and inducing flow oscillations. According to Swiegers et al[19] the accumulation of bubbles on the electrode surface formed a bubble curtain, hindering electrolyte access to the electrode and reducing electrolysis efficiency. The methods for enhancing bubble detachment can be classified into active and passive approaches [20]. Better

E-mail address: mxj@ncepu.edu.cn (X. Ma).

^{*} Corresponding author.

Nomer	Nomenclature		Thickness of the plates, mm
Α	Surface area, mm ²	Greek symbols	
$E_{ m L,k}$	Liquid kinetic energy, J	δ	Displacement, m
$E_{\mathrm{P.k}}$	Plate kinetic energy, J	γ	Mobility, m ³ ·s/kg
$E_{\mathrm{B.k}}$	Bubble kinetic energy, J	ρ	Fluid density, kg/m ³
$E_{\rm e}$	Elastic potential energy, J	$ ho_0$	Initial mass density, kg/m ³
$E_{\text{L.k}}$	Liquid kinetic energy, J	θ	Contact angle, °
$f_{\scriptscriptstyle m S}$	Surface tension vector, N/m ³	$ heta_a$	Advancing contact angle, °
$F_{ m V}$	Volumetric force, N	θ_r	Receding contact angle, °
F	Deformation gradient, N	σ	Surface tension coefficient, N/m
$F_{ m V}$	Volumetric force, N	ϕ	The phase field variable
g	Gravitational acceleration vector, m/s ²	ψ	Phase field auxiliary variable
h	Height, mm	μ	Fluid density, Pa·s
I	Unit matrix	λ	Mixing energy density, N
Δl	Contact length, mm	ε	Interfacial thickness, m
1	Length, mm	β	Morphology factor
n	Outward normal vector	$\Delta\delta$	The change in deflection of the free end of the plate
p	Pressure of fluid, Pa	Abbreviation	
$R_{\rm a}$	Surface roughness, µm	CAH	Contact angle hysteresis
R	Bubble's equivalent diameter, mm	ER	Elastic Region
S	Piola-Kirchhoff stress tensor	ORR	Quasi-Rigid Region
t_c	THE time of the bubble moves through the channel, ms	Ųκκ	Quasi-rigiu region
$\Delta t_{ m d}$	Bubble departure time, ms	Subscript	
$\Delta t_{ m de}$	TOTAL bubble motion time, ms	В	Bubble
$\Delta t_{ m r}$	Bubble residence time, ms	max/min	Maximum/minimum
$oldsymbol{u}_{ m tr}$	Solid velocity, m/s	x	Along the <i>x</i> -axis
u	Velocity vector, m/s	y	Along the <i>y</i> -axis
и	Velocity, mm/s	-	
$v_{\rm n}$	Needle injection velocity, mm/s		

performance is obtained by active approaches due to the external energy supply [21]. Passive methods are much more popular due to their simplicity and wide use. Okech and Chen et al[22,23] investigated bubble movement in tapered channels. They found that bubble deformation creates a capillary pressure gradient, enabling spontaneous bubble motion without the need for external driving forces. Turkoz and Swiegers et al[19,24] investigated the use of porous media surfaces to promote bubble detachment. They found that bubbles moved outward due to capillary forces. However, a larger pressure drop was also induced through the above methods, which would lead to high energy consumption and operational costs [25]. Forces acting on bubbles in two-phase flow in the vertical direction can be categorized into two classes [26–28]. One is forces that prevent bubble detachment, such as surface tension, drag force, and Marangoni force [29,30]. The other is driving forces that promote bubble detachment, primarily driven by buoyancy, including shear lift force and contact pressure force [31,32]. Bubbles detache from the surface when the force balance is broken. Many studies aim to improve bubble dynamics by adjusting the relative magnitudes of driving and inhibitory forces. Angulo and Wang et al[33, 34] also demonstrated that micro-nanostructured surfaces can significantly enhance bubble detachment. Bubble departure time decreased by 94 % due to the permeability and roughness of the nanoarray. Several scholars found that the bubble period was shortened by adding surfactants [35-38]. Surface tension acting on the bubble interface and the surface tension gradient are decreased due to surfactants. The decrease in surface tension gradient led to a reduction in the Marangoni force [39]. Additionally, the adsorption of surfactant molecules at the liquid-vapor interface slowed the bubble coalescence due to the repulsive force. Consequently, more bubbles detached in the form of smaller bubbles. Xu and Yu et al[40,41] studied gas-liquid two-phase flow in a confined space using nanofluids. They found that nanoparticles reduce bubble diameter and prevent blockage by lowering surface tension and

inhibiting coalescence. But the performance of nanofluids and surfactants depends strongly on channel dimensions and working fluid properties, and nanofluid deposition can affect the stability of gas-liquid two-phase flow [42]. The above-mentioned literature indicates that researchers have been actively pursuing improvements in bubble dynamics within confined space, achieving significant advancements. However, surface tension is inherently limited. Consequently, any approach such as modifications aimed at enhancing bubble dynamics through surface tension has a restricted impact on the overall improvement of bubble dynamics. Specifically, the enhancement achieved by altering surface tension is minimal when using working fluids with inherently low surface tension [43]. An innovative technique had been introduced by Laskar and Das [44], which involved the shearing of bubbles through liquid jet impingement over the heated surface. It effectively addressed bubble blockage caused by coalescence in confined space. High bubble departure frequency was obtained due to the early necking effect. A maximum enhancement of 25 % in heat transfer was observed in their study. A recent study of the flow boiling performance of a novel pin - fin array using jet impingement technology by Camarasa [45] also found that bubble blockage was reduced, resulting from large bubble breakup and departure. However, an effective passive way for bubble removal strategies is much more popular in industrial application.

Exploring energy inside two-phase flow system to improve bubble dynamics has become a promising approach. Meng [46] invented a novel micro-pump to support liquid transport in micro-channels. Surface energy gradients were used to direct bubble removal. Previous studies have primarily focused on the bubble dynamics in channels coated with micro/nano-structures, which are typically fabricated from rigid materials such as silicon and copper [47,48]. In such rigid channels, wall deformation is negligible, and bubble behavior is mainly governed by surface characteristics, such as wettability and surface roughness [49].

Elastic modulus is an unnoticed parameter in their studies. However, recent studies have shown that bubble motion could be modulated and accelerated by elasticity [50]. The elastic effect on bubble dynamics in channel should be investigated. Ma et al [51,52] proposed a novel way to promote bubble detachment through the oscillation of a pair of flexible fins in pool boiling system. Detailed bubble dynamics including nucleation process was investigated. Bubble cycle period is compared among cases with different bending rigidity. The results demonstrated that the frequency of bubble detachment and the ascending velocity of bubbles within the channel were maximally enhanced by 86 % and 17 %, respectively. Better pool boiling performance was obtained by the case with the flexible plates due to the plate movement. Elastic potential energy was converted into the bubble kinetic energy. This is a novel way to promote bubble departure and improve heat transfer performance. However, the detailed energy conversion mechanism and the effect of elastic modulus on bubble dynamic during the bubble departure process was not discussed. Bubble interaction with flexible plates has great potential in bubble manipulation [53,54]. The detailed energy conversion during bubble departure process should be investigated in detail.

This study numerically examines bubble dynamics between plates with varying elastic modulus, with experimental validation. For the first time, the interaction between elastic plate dynamics and bubble behavior is explored. The influence of elastic modulus on bubble total motion time, which includes bubble residence time (the time when bubbles reside in the elastic channel) and bubble departure time (the time when bubbles depart from the tip of elastic plates) is thoroughly analyzed. The kinetic and elastic potential energy variations during the interaction between the bubble and elastic plate are presented and discussed. A novel mechanism is proposed, where the bubble itself provides energy for departure via induced elastic plates. Fascinating plate morphologies, such as necked-in and necked-out shapes, are observed and shown to enhance bubble departure. Furthermore, a quantitative design guideline for elastic plates is introduced. This work aims to contribute significantly to the design of microfluidic systems, which would benefit the mass transfer, and provides a theoretical basis and technical support for the design of boiling surfaces in confined space and the heat exchanger.

2. Experiments and methods

2.1. Geometric model and meshing

In this paper, the 2-D transient dynamics of a single bubble rising within a flexible channel were simulated using COMSOL Multiphysics 6.0 software by using dynamic mesh technique. To validate the feasibility of the two-dimensional model, a representative three-dimensional case with consistent boundary and initial conditions was constructed. Both models utilized physics-controlled meshing. As shown in Fig. 2(a), the evolution of bubble rise velocity in 2D and 3D simulations showed good agreement, with an average relative error of 4.69 %, confirming that the 2D simulation accurately captures the essential bubble dynamics. Additionally, the 3D simulation took approximately twenty-four times longer than the 2D one, highlighting the efficiency advantage of the 2D model.

The schematic of the geometrical model is shown in Fig. 1. The upper section of the channel was designated as the pressure outlet, while the remaining boundaries were defined as no-slip walls. Dual flexible plates (10 mm \times 0.2 mm) with a spacing of 1.2 mm were symmetrically arranged in a rectangular computational domain (60 mm \times 30 mm). The bottom of each solid plate was constrained with a fixed boundary condition to simulate clamped ends, while other boundaries of the plates were defined as no-slip walls. A contact angle of 30° was applied at the solid-fluid interfaces. A velocity inlet with a fluid inflow velocity of 0.05 m/s was imposed at the bottom of the channel. Gas or liquid alternately entered from the boundary at certain time intervals, defining $\phi=-1$ for fluid 1 (water) and $\phi=1$ for fluid 2 (air bubble).

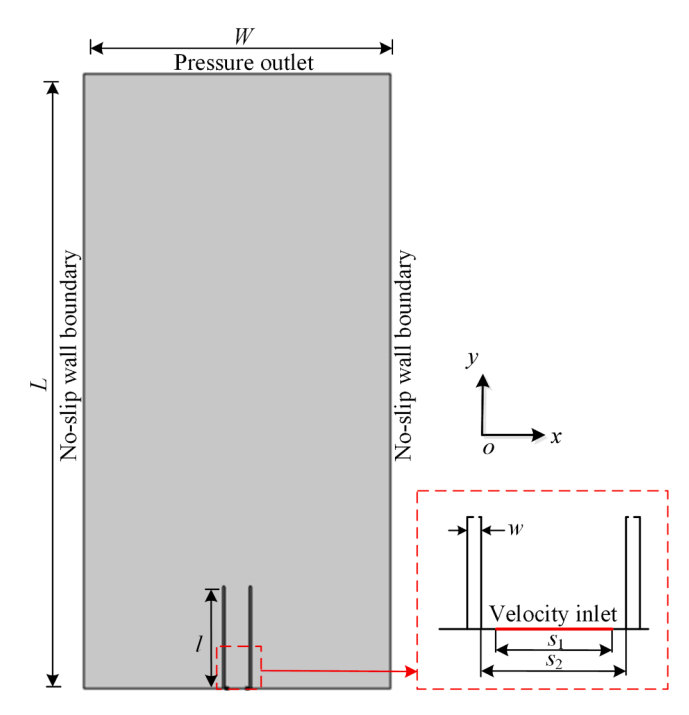


Fig. 1. Computation domain.

$$\phi = \begin{cases} 1, & 0 < t \le 0.1 \\ -1, & 0.1 < t < 0.8 \end{cases}$$
 (1)

The entry order and timing of the fluid were controlled by the inlet function, represented as a rectangular wave function of the phase field variable ϕ over time [55]. The volume of an individual air bubble remained constant across the channel with varying elastic moduli. Table 1 presents the material properties of the plates and the liquid. The elastic modulus of the plates spans $E \in [2 \times 10^6, 2.06 \times 10^{11}]$ Pa, with 2.06×10^{11} Pa being the elastic modulus of steel, selected for the rigid channel. The impact of elastic modulus on bubble dynamics is investigated when the contact angle is 30° , during the phase when a bubble fully detaches from the flexible channel.

The isothermal incompressible Navier-Stokes (N-S) equations were used to describe the two-phase flow system, where the mass and momentum equations were solved by the finite volume method in the Cartesian coordinate system. The N-S equations consider the average properties of the two fluids, and the above equations were described as follows:

Mass equation:

$$\nabla \boldsymbol{u} = 0 \tag{2}$$

Momentum equation:

$$\rho\left(\frac{\partial \boldsymbol{u}}{\partial t} + \boldsymbol{u} \cdot \nabla(\boldsymbol{u})\right) = -\nabla p + \nabla \cdot \left(\mu\left(\nabla \boldsymbol{u} + (\nabla \boldsymbol{u})^{T}\right)\right) + \rho \boldsymbol{g} + \boldsymbol{f}_{s}$$
(3)

In Eqs (2)-(3), ρ and μ denote the fluid density and the dynamic viscosity, respectively, kg/m³ and Pa·s; \boldsymbol{u} and p denote the velocity vector and the pressure of fluid, respectively, m/s and Pa; \boldsymbol{g} is the gravitational acceleration vector, m/s²; and \boldsymbol{f}_s represents the surface tension vector, N/m³.

Table 1Material properties.

	density /kg·m ⁻³	poisson's ratio	elasticity modulus /Pa
Solid Air Water	1000 1.25 998	0.3 1×10^{-5} 1×10^{-3}	$[2 \times 10^6, 2.06 \times 10^{11}]$

The phase field variable ϕ is introduced to describe the physical state at each location in space and time in the phase field method. The value of ϕ ranges between [-1, 1]. It equals -1 and 1, corresponding to the two fluids, respectively, and indicates the interface in the range of (-1, 1) [56].

The two-phase fluid interface actually consists of a very thin region, which decomposes the Cahn-Hilliard equation into two second-order partial differential equations:

$$\frac{\partial \phi}{\partial t} + \nabla \cdot \mathbf{u}\phi = \nabla \cdot \frac{\gamma \lambda}{e^2} \nabla \psi \tag{4}$$

$$\psi = -\nabla \cdot \varepsilon^2 \nabla \phi + (\phi^2 - 1)\phi \tag{5}$$

In Eqs. (4)-(5), t is the time and u is the fluid velocity, ψ denotes the phase field auxiliary variable; γ is the mobility, $m^3 \cdot s/kg$; $\gamma = \chi \varepsilon^2$, λ and ε represent the mixing energy density and the interfacial thickness proportional to the capillary width, respectively, N and m, and λ and ε are related to the surface tension coefficient σ (N/m) as follows [57]:

$$\sigma = \frac{2\sqrt{2}}{3} \frac{\lambda}{\varepsilon} \tag{6}$$

The motion equations of solid mechanics were given by Newton's second law:

$$\rho_0 \frac{\partial^2 \delta}{\partial t^2} = \nabla_x (FS) + F_V \tag{7}$$

$$\mathbf{F} = \mathbf{I} + \nabla \delta \tag{8}$$

where F and S are the deformation gradient and Piola-Kirchhoff stress tensor, respectively; F_V denotes the volumetric force component in the current configuration relative to the undeformed volume; ρ_0 and δ represent the initial mass density and the solid displacement, respectively, kg/m³ and m [58], and I is the unit matrix.

The fluid-solid coupling boundary is introduced. The force in the fluid-solid coupled system consists of the fluid force:

$$f = \mathbf{n} \cdot (-p\mathbf{I}) + \mathbf{n} \cdot \left(\mu \left(\nabla \mathbf{u} + (\nabla \mathbf{u})^T \right) - \frac{2}{3} \mu (\nabla \mathbf{u}) \mathbf{I} \right)$$
(9)

where n is the outward normal vector perpendicular to the boundary. This force is applied to the solid boundary through the fluid-solid coupling boundary in the form of a Lagrangian volumetric force F_V . The velocity coupling consists of the solid velocity $u_{\rm tr}$, and acts as a moving boundary on the fluid side through the fluid-solid coupling boundary:

$$u_{tr} = \frac{\partial \delta}{\partial t} \tag{10}$$

A global triangular unstructured mesh was built as shown in Fig. 2(b) with the maximum mesh size of 0.84 mm and the mesh growth rate of 1.1. The contact region between the bubble and the plates was divided into smaller mesh scales to capture the interaction between the bubble and the flexible channel. To better ensure accuracy and to capture the details of plates deflection, local encryption was carried out between flexible channels and their vicinity, with the mesh size of 0.012 mm.

Two flexible plates with an elastic modulus of 7×10^6 Pa and 2.06×10^6 10¹¹ Pa were selected for mesh-independence verification, and the grid numbers were all between 15,000 and 70,000. Two representative elastic moduli, $E=7\times 10^6$ Pa and $E=2.06\times 10^{11}$ Pa, were selected to ensure the accuracy and reliability of simulation results across different elastic modulus conditions. The effect of different grid numbers on bubble departure time (Δt_{de}) is shown in Fig. 2(c). Considering the accuracy and time computational cost of the model, the grid number of 41,286 is used in this model. Also, a time independence test is conducted to assess the stability and consistency of a numerical simulation over different time steps. The evolution of bubble kinetic energy under different time steps (0.01 s, 0.001 s, and 0.0001 s) was verified as shown in Fig. 2(d). The relative error between results for 0.0001 s and 0.001 s is < 9.29 % throughout the simulation, while larger relative error of 40.81 % appears at 0.01 s during the later stage. The time step of 0.001 s was adopted as the uniform time step for all simulations.

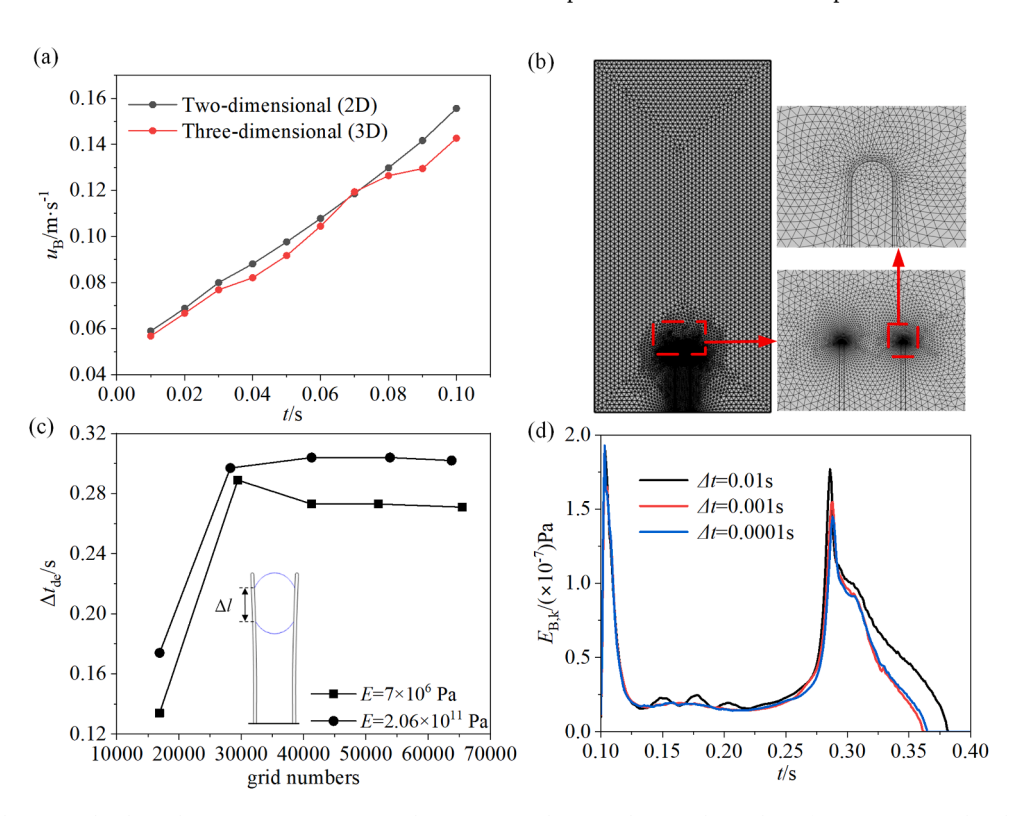


Fig. 2. Validation and numerical independence tests. (a) Comparison between 2D and 3D simulations, (b) mesh configuration, (c) mesh-independence test and (d) time-independence test.

2.2. Model validation

To validate the computational model and methodology used in this research, experiments were conducted to observe the rising and detachment behavior of a single bubble within a channel. The experimental setup included a transparent glass chamber, a high-speed video camera, a micro syringe pump, and a needle (refer to Fig. 3 for details). Stainless steel 304, with an elastic modulus of 2×10^{11} Pa and a density of 1370 kg/m³, was employed as the flexible plate material. The flexible plate stiffness was varied by changing the thickness of the plates. The thickness of the plates w = 0.01 mm (stiffness $EI = 1.5 \times 10^{-7}$ N/m) and w = 0.5 mm ($EI = 1.875 \times 10^{-2} \text{ N/m}$) was selected to explore flexible and rigid plates, respectively, and the dual flexible plates (10 mm (z) \times 9 mm $(x) \times w(y)$) were arranged symmetrically and parallel to each other with a spacing of 1.2 mm to form a flexible channel and a rigid channel. We performed a hydrophilic modification treatment on the 304 stainless steel. After the modification of wettability, the 304 had a surface roughness of $R_a = 0.94 \,\mu\text{m}$ and a contact angle $\theta_{CA} = 12.8^{\circ}$. To ensure comparability between simulation and experimental results, the numerical simulations employed a contact angle of 12.8° consistent with experiments during validation. However, a contact angle of 30° was uniformly adopted in subsequent numerical analyses to better reflect typical wetting conditions encountered in practical applications, thus enabling the simulations to capture more generally representative bubble dynamics.

The stainless-steel plates were sequentially cleaned with acetone, alcohol, and deionized water for 10 min prior to each experiment. To ensure precise control of the channel spacing, a septum with a thickness of 1.2 mm was positioned at the base of the stainless-steel plates and secured using two rectangular rigs. A needle with a diameter of 0.45 mm, connected to a micro syringe pump, was placed at the bottom of the channel. The entire experimental setup was submerged in a glass chamber filled with deionized water. To ensure clear visualization of the channel's opening and closing process and bubble motion during the experiment. Air was injected into the channel at a flow rate of 5 $\mu\text{m/s}$ using the syringe pump, with an error of 0.5 %. A high-speed camera (MotionPro Y4, IDT, USA) operated with a frequency of 2000 Hz, focused on an area of 1016 × 1016 pixels and provided a spatial resolution of 13.7 μ m and the statistical centroid height of bubbles (h_b) change exceeded 0.38 mm, with a maximum error in bubble velocity of 3.6 % as calculated by $\delta h/h = 137/3800 = 3.6$ %. Table 2 summarized the uncertainties of various parameters.

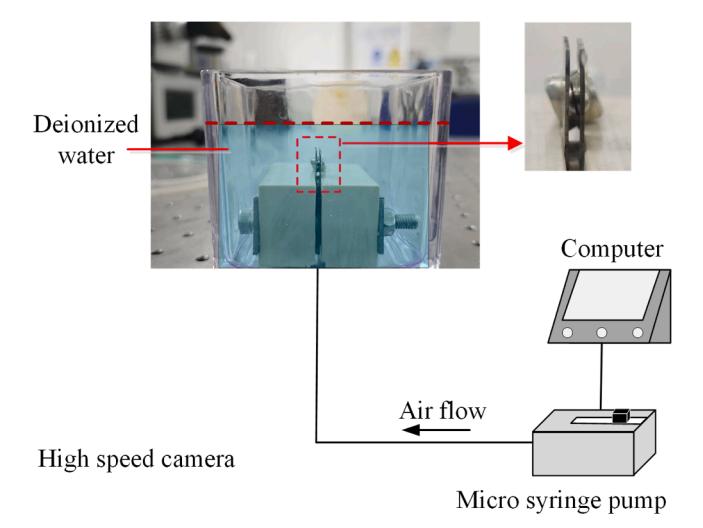


Fig. 3. Experimental setup.

Table 2Parameter uncertainties.

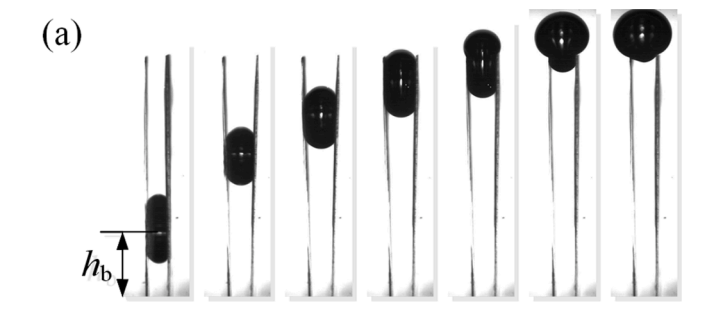
Parameters	Error
Needle injection velocity v_n (μ m/s)	0.5 %
Bubble height h_b (mm)	3.6 %

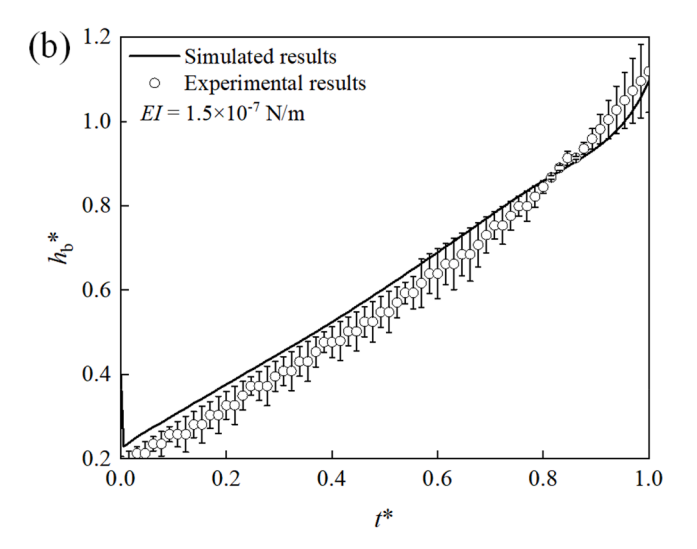
3. Results and discussion

For the sake of validation, the experimental data are compared with the results obtained from the numerical simulations introduced in the previous sections as shown in Fig. 4. Fig. 4(a) showed an experimental image of a bubble moving through the elastic channel. As the bubble rose, the fins first opened and then closed. We defined h_b as the centroid height of the bubble, normalized it to $h_b^* = h_b/l$, and compared it with the simulation under the same EI, as shown in Fig. 4(b) and Fig. 4(c). The results showed that the numerical results exhibited a good qualitative and quantitative agreement with the experimental data. The maximum discrepancy for the rigid plates is 6.47 %, and for the flexible plates is 9.76 %. The error between simulation and experimental results is <10 % for both rigid and flexible channels, indicating the reliability of the numerical simulation. In the case of flexible plates, the deviation between simulation and experimental results is more significant, particularly during the early stage of bubble rising (0 s < t < 0.2 s). During this stage, the flexible walls undergo considerable deformation driven by the bubble, and their nonlinear structural response is highly sensitive to variations in fluid-structure interaction boundaries. In the experiments, factors such as fabrication tolerances, local stiffness heterogeneity, and slight geometric asymmetries may cause deviations from the idealized simulation boundaries, leading to larger discrepancies. In contrast, the structural response under rigid plate conditions is minimal, making the simulation results less susceptible to these influences and thus more consistent with the experimental observations.

The dynamics of both the bubble and the plates, during the upward movement of the bubble between flexible channels with varying elastic moduli, are illustrated in Fig. 5. The bubble exhibited a deformed morphology as it ascended between flexible elastic walls ($E=7\times10^6$ Pa), whereas it followed a plug flow pattern between fixed rigid plates (E $= 2.06 \times 10^{11}$ Pa), as illustrated in Fig. 5(a). Using the bubble dynamics between walls with $E = 7 \times 10^6$ Pa as an example, the displacement (δ) of the flexible walls displayed a periodic variation, as depicted in Fig. 5(b). The flexible plates expanded during the bubble's upward motion, reaching a maximum displacement of $\delta = 0.82$ mm at $t_{\delta max}$. Then, the displacement decreased as the distance between the walls diminished during the later stages of the bubble's ascent. The minimum displacement, δ , occurred at $t_{\delta \min}$ after the bubble's departure, as shown in Fig. 5 (b). While the maximum displacement increased as the elastic modulus decreased, the plate with the lowest elastic modulus did not exhibit the largest displacement. For instance, during the initial movement, the displacement of plates with $E=7\times 10^6$ Pa was greater than that of plates with $E=2\times 10^6$ Pa. This observation suggests that plate dynamics are influenced by the coupling interaction between the bubble and the plates, a phenomenon further explored in Figs. 7 and 8.

In addition to the plate displacement along the x-axis, the contact length (Δl) between the bubble and the plate was calculated for cases with varying elastic moduli and is shown in Fig. 5(c). Zhang [50] highlighted the influence of contact line length on bubble dynamics in their study of bubbles on anisotropic slip cilia surfaces. In their simulations, the contact line length was treated as one of the auxiliary parameters used to interpret variations in bubble motion, such as slip direction and velocity changes. However, their study did not analyze the contact line length as a primary variable, nor did it report any quantitative or trend-based discussion regarding its non-monotonic evolution. Inspired by this work, we quantitatively examined the contact length (Δl) between the bubble and the flexible plates in our current setup, as illustrated in Fig. 5(c). As observed in the figure, the contact length





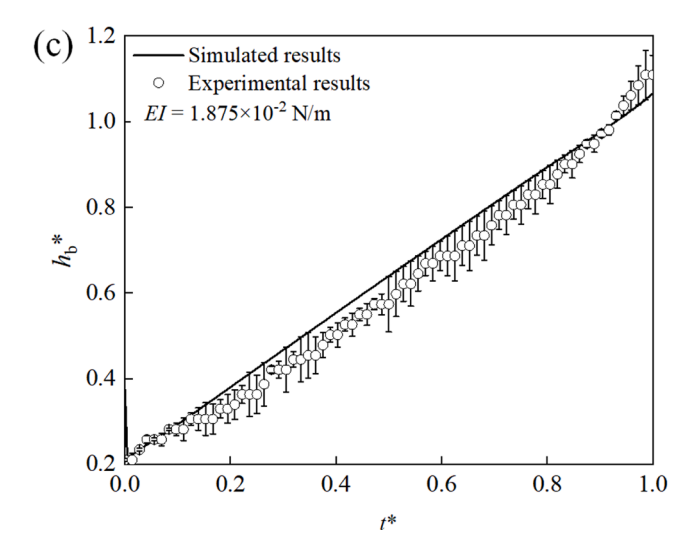


Fig. 4. Validation of simulation with experimental results. (a) Experimental snapshots of bubble motion in a flexible channel with $EI=1.5\times10^{-7}$ N/m, (b) Comparison on h_b^* for case with $EI=1.5\times10^{-7}$ N/m between simulation and experimental results (flexible plates) and (c) Comparison on h_b^* for case with $EI=1.875\times10^{-2}$ N/m between simulation and experimental results (rigid plates).

decreased during the initial stage for all cases. However, distinct trends emerged during the mid-stage of the variation: for plates with high elastic modulus ($E > 1 \times 10^7$ Pa), the contact length stabilized around a constant value, while for plates with low elastic modulus ($2 \times 10^6 \le E \le 1 \times 10^7$ Pa), the contact length first decreased until $t_{\delta max}$, then increased until t_c . In both scenarios, the contact length decreased during the final stage when the bubble began detaching from the plate tips. This indicates

the presence of a non-monotonic variation in the contact length for cases with low elastic modulus. Interestingly, this coincides with a non-monotonic variation in the total motion time (Δt_{de}) for plates with elastic moduli ranging from 2×10^6 to 1×10^7 Pa, as illustrated in Fig. 5 (d). Notably, the range of elastic modulus showing this non-monotonic behavior is the same for both contact length and total motion time. Based on these findings, we propose a classification of elastic regions: The elastic plates with an elastic modulus in the range of 2×10^6 Pa to 1×10^7 Pa are defined as the Elastic Region (ER), characterized by non-monotonic behavior. Conversely, the plates with an elastic modulus greater than 1×10^7 Pa are classified as the Quasi-Rigid Region (QRR).

A minimum bubble departure time was observed for the case where $E=7\times10^6$ Pa as shown in Fig. 5(d). Compared to the total motion time for the bubble passing through rigid walls, a significantly shorter period was noted for its motion between flexible walls. However, this does not imply that the bubble moved faster between flexible walls with a lower elastic modulus. The total motion time, $\Delta t_{\rm de}$, only increased with a higher elastic modulus when $E>7\times10^6$ Pa. For bubble motion between flexible walls with a low elastic modulus (2×10^6 Pa 2×10^6 Pa), an optimal elastic modulus (2×10^6 Pa) was identified, resulting in the shortest bubble motion period. It should be noted that the total motion time is also calculated for infinite space without plates. It is 0.143 s for infinite space which is much shorter than that in confined space. These results highlight the importance of enhancing bubble detachment efficiency in confined environments.

Based on the characteristics of contact line variations and the total bubble departure time across different elastic modulus cases, Fig. 6 illustrates the bubble dynamics for three elastic modulus regions: the Elastic Region (ER, $2 \times 10^6 \le E \le 1 \times 10^7$ Pa), the Quasi-Rigid Region (QRR, $1 \times 10^7 < E < 2.06 \times 10^{11}$ Pa), and the Rigid Wall ($E = 2.06 \times 10^{11}$ Pa). This includes the maximum bubble tip height, $h_{\rm max}$, during the bubble movement process. The whole bubble evolution process $\Delta t_{\rm de}$ is divided into two stages based on its spatial position: (i) the residence stage Δt_r (0- t_c), during which the bubble rises within the channel, and (ii) the departure stage Δt_d (t_c – t_{de}), during which the bubble moves from the moment when its top reaches the tip of the channel to the moment of its departure. It was observed in Fig. 6(b) that the bubble residence time $\Delta t_{\rm r}$ decreased with increasing elastic modulus, whereas the departure time Δt_d exhibited an increasing trend. For all cases, the bubble residence time Δt_r accounted for a substantial portion of the entire cycle (> 79.3 %). A longer residence time could enhance mass transfer in various applications [59,60]. However, the total bubble motion time Δt_{de} decreased for cases with a low elastic modulus, primarily due to the shorter bubble departure time Δt_d . Specifically, for bubble motion between plates with $E=7\times10^6$ Pa, the bubble total motion time $\Delta t_{\rm de}$ was reduced by 10.2 % compared to that for rigid walls ($E = 2.06 \times 10^{11} \text{ Pa}$), with the bubble departure time Δt_d decreasing by 63.5 % relative to the rigid cases.

It can be concluded that the reduction in bubble departure time resulted in a shorter overall process duration for cases involving flexible walls. The mechanism responsible for the reduced departure period in cases with elastic plates was analyzed here. Four different elastic moduli (E = 7 \times 10⁶, 3 \times 10⁷, 5 \times 10⁷, and 2.06 \times 10¹¹ Pa) were selected to compare the bubble departure characteristics during the detachment stage ($t_c \sim t_{de}$), where t_c is represented by empty dots, and t_{de} by solid dots, as shown in Fig. 7. A significant increase in bubble velocity along the y-axis (u_B ,y) was observed for cases with a low elastic modulus (E = 7× 10⁶ Pa) during the detachment stage, as illustrated in Fig. 7(a). The highest bubble velocity occurred in the case with the lowest elastic modulus ($E = 7 \times 10^6$ Pa), whereas the velocity remained nearly constant for rigid walls during this stage. As seen in Fig. 5(b), the plate displacement (δ) dropped sharply between t_c and t_{de} , enabling the calculation of elastic potential energy (E_e) and bubble kinetic energy (E_B). k) during the bubble detachment process.

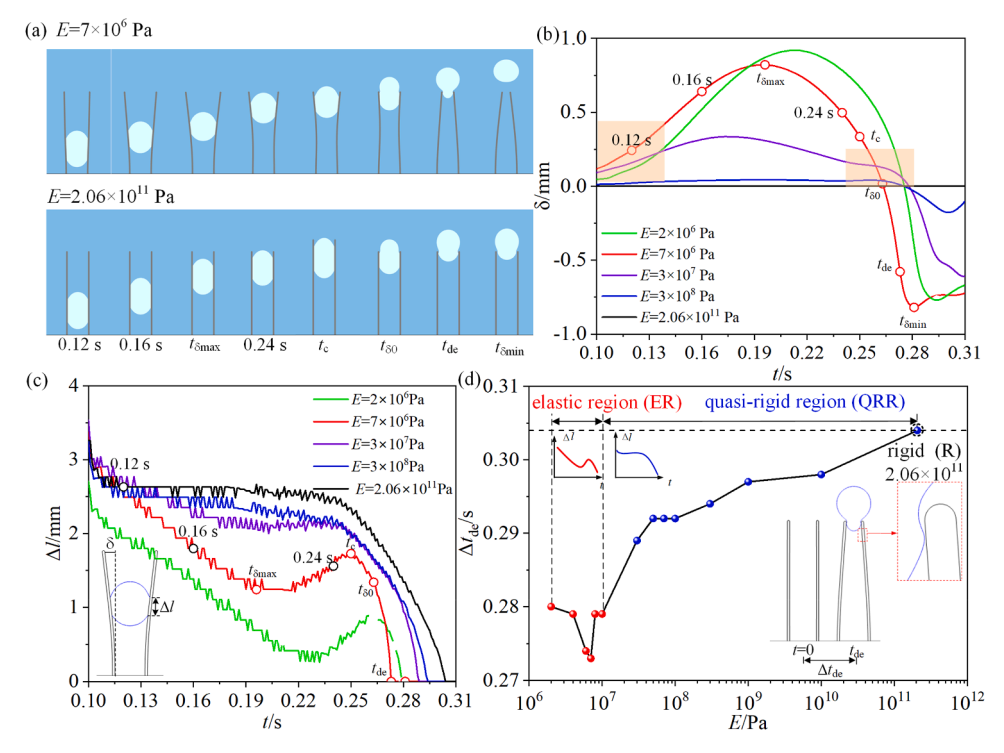


Fig. 5. Bubble dynamics in a deformable channel. (a) case with $E = 7 \times 10^6$ and 2.06×10^{11} Pa, (b) the plate displacement in x axis, (c) the contact length between the bubble and walls and (d) the bubble departure time.

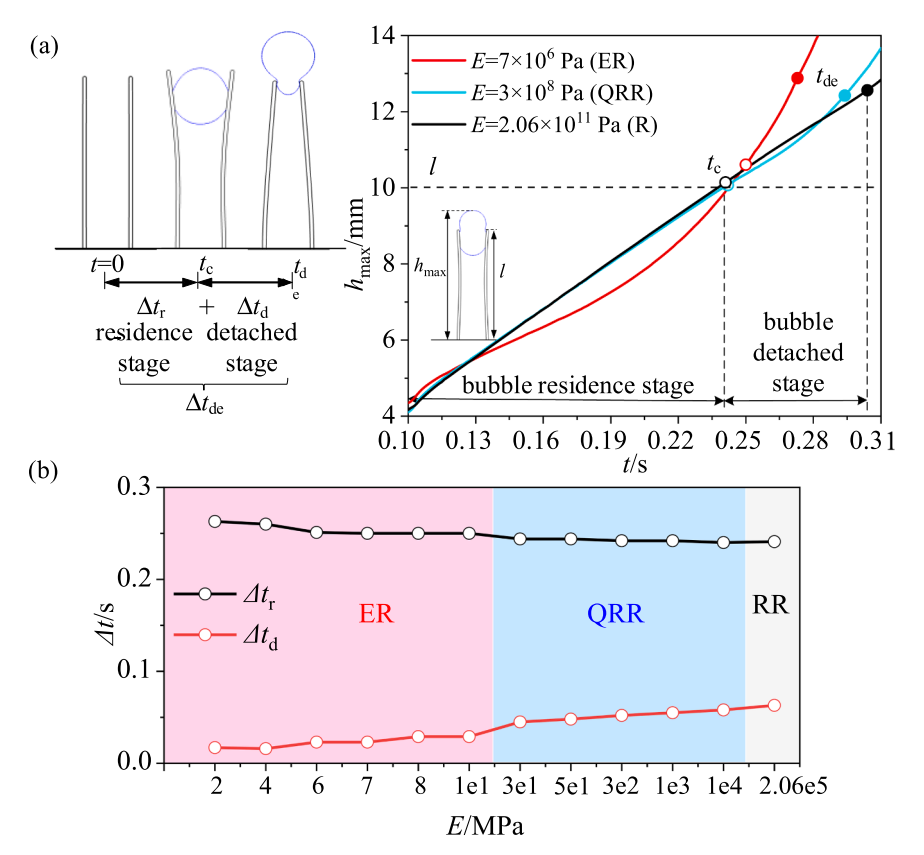


Fig. 6. Bubble dynamics between plates with different elastic moduli. (a) the height of the bubble tip and (b) bubble cycle.

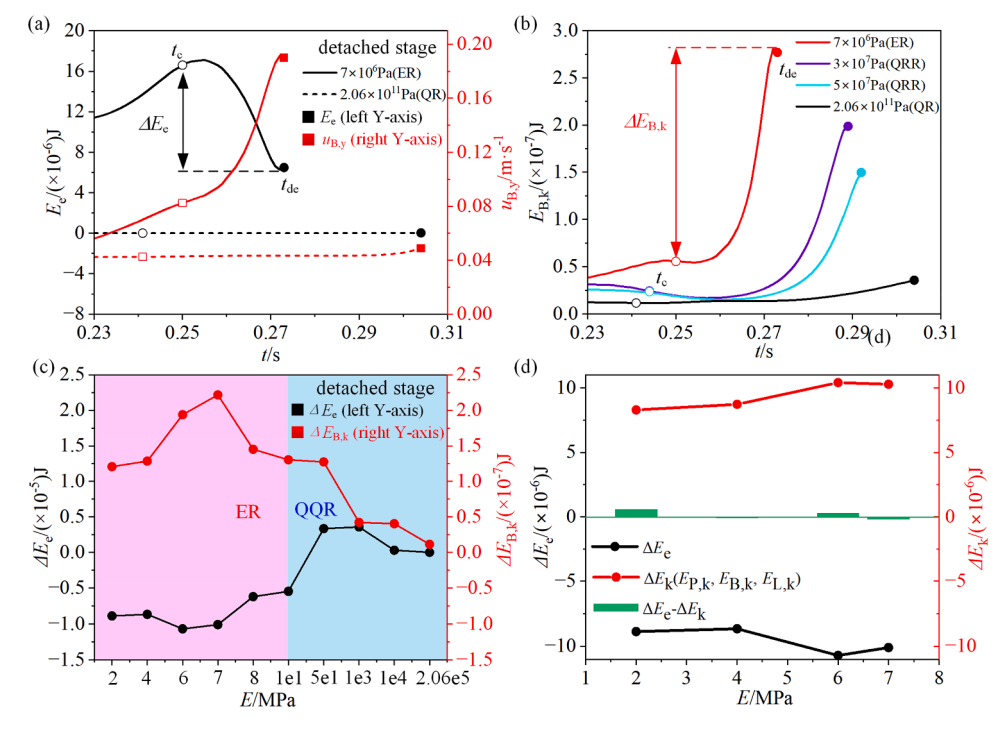


Fig. 7. Energy conversion in bubble detachment stage. (a) bubble velocity in *y*-axis and elastic potential energy, (b) bubble kinetic energy, (c) energy changes and (d) elastic potential energy and system kinetic energy ($E = \frac{2}{4}$ /6/7 MPa).

$$Ee = \int \left[\frac{1}{2} \frac{E(1-\nu)}{(1+\nu)(1-2\nu)} * \left(\left(\frac{\partial u}{\partial X} \right)^2 + \left(\frac{\partial v}{\partial Y} \right)^2 \right) \frac{1}{4} \frac{E\left(\frac{\partial u}{\partial Y} + \frac{\partial v}{\partial X} \right)^2}{(1+\nu)} + \frac{E\nu\left(\frac{\partial u}{\partial X} + \frac{\partial v}{\partial Y} \right)}{(1+\nu)(1-2\nu)} \right] dAP$$

$$(11)$$

$$E_{B,k} = \int \frac{1}{2} \rho_B \Big(u_x^2 + u_y^2 \Big) dA_B \tag{12}$$

Where E and ν are the elastic modulus and Poisson's ratio of the elastic plate, respectively. The terms u and v are the strain components in the X- and Y-directions, respectively. A_P is the surface area of the elastic plates, A_B is the surface area of bubble and ρ_B is the gas density. u_x and u_y are the velocities in the x- and y-axes, respectively. The elastic potential energy (E_e) decreased significantly in the elastic region during the detachment stage, as illustrated in Fig. 7(a). In contrast, for the rigid case ($E = 2.06 \times 10^{11}$ Pa), the elastic potential energy remained nearly constant. Meanwhile, the bubble's kinetic energy displayed an opposite trend, as shown in Fig. 7(b). The substantial increase in the bubble's kinetic energy was attributed to the considerable release of elastic potential energy from the plate in the elastic region. The variations in bubble kinetic energy and elastic potential energy during the detachment process for all cases are depicted in Fig. 7(c). It was observed that a portion of the elastic potential energy ($\Delta E_{\rm e}$) was converted into bubble kinetic energy ($\Delta E_{B,k}$) during this process. This conversion was notably greater for cases within the elastic region (2 \times 10⁶ Pa \leq $E \leq$ 1 \times 10⁷ Pa), highlighted in pink. The release of elastic potential energy from flexible plates contributed to shorter bubble departure time. The energy conversion in this process was analogous to the springboard effect observed when a droplet impacts an elastic substrate [61]. From Fig. 7(c), it is observed that the released elastic potential energy was only partially transformed into the bubble's kinetic energy during the detachment stage. To further evaluate the energy conversion efficiency, the total kinetic energy of the system, including the kinetic energy of the bubble

 $(E_{\rm B,k})$, the flexible plates $(E_{\rm P,k})$, and the surrounding liquid $(E_{\rm L,k})$ was calculated. The results under different elastic moduli (E=2,4,6, and 7 MPa) are presented in Fig. 7(d). In this figure, the green bars represent the difference between the released elastic energy and the total kinetic energy $(\Delta E_{\rm e} - \Delta E_{\rm k})$. It is evident that the difference is minimal, indicating a highly efficient conversion of elastic potential energy into system kinetic energy. The individual kinetic energy components were computed using the following equations:

The liquid kinetic energy $E_{L,k}$:

$$E_{L,k} = \int \frac{1}{2} \rho_L (u_x^2 + u_y^2) dA_L$$
 (13)

The plate kinetic energy $E_{P,k}$:

$$E_{P,k} = \int \frac{1}{2} \rho_P (u_x^2 + u_y^2) dA_P$$
 (14)

The bubble surface energy E_s :

$$E_{s} = \sigma(\Delta A_{1} + \Delta A_{2}) + \sigma \cos \theta_{w} \Delta A_{3}$$
(15)

 ΔA_1 and ΔA_2 represent the surface areas of the upper and lower gasliquid interfaces, respectively, while ΔA_3 denotes the surface area of the gas-solid interface. The static contact angle (θ_ω) is defined as $\theta_\omega=\pi/6$. During the bubble detachment process, the plate gradually returned to its original state as the stored elastic potential energy was released. This release resulted in increased movement speeds of both the plate and the fluid. It was observed that the majority of the released energy was converted into the kinetic energy of the liquid.

Interestingly, cases with the lowest elastic modulus (e.g., $E=2\times10^6$ Pa) did not exhibit the highest energy storage. Energy storage was influenced by the bubble motion process during the bubble residence time. Understanding the bubble motion process for cases with smaller elastic moduli ($E<1\times10^7$ Pa) in the earlier stage was essential. The bubble velocity along the *y*-axis ($u_{\rm B}$,y) during the residence time is shown in Fig. 8(a). It was observed that the bubble's velocity in the *y*-axis between flexible plates initially decreased and then increased during the residence time. For plates in the elastic region ($2\times10^6\le E\le1\times10^7$ Pa), the velocity variation changed significantly, decreasing as

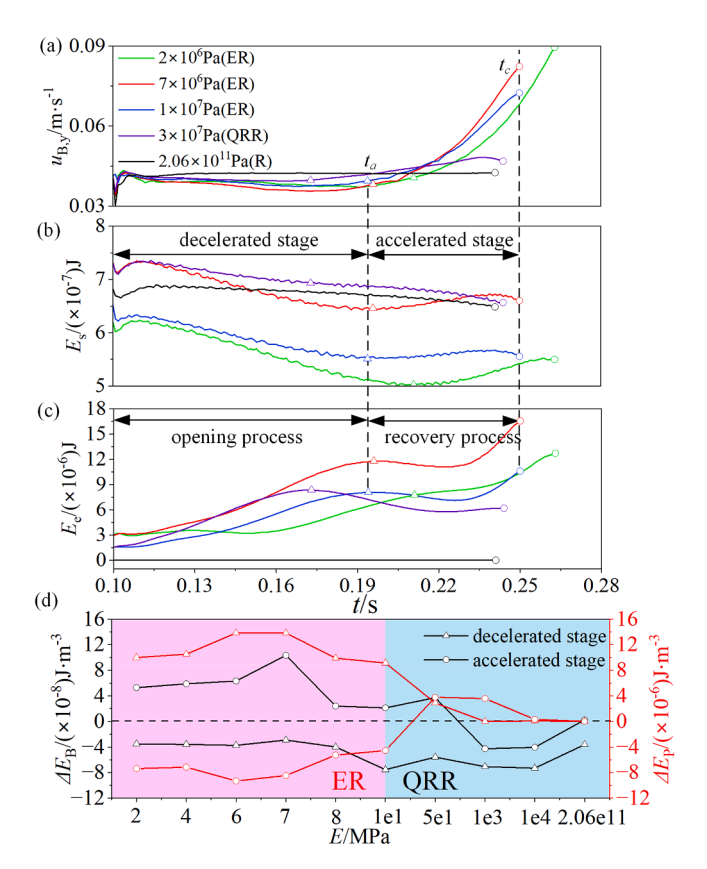


Fig. 8. Energy conversion in the bubble residence stage. (a) bubble velocity in y-axis, (b) bubble surface energy, (c) elastic potential energy and (d) energy changes.

elasticity increased. In contrast, the bubble velocity along the y-axis between rigid plates remained nearly constant ($\Delta u_{B,y} < 0.015$ m/s in the residence stage, and $\Delta u_{\rm B,v} > 0.015$ m/s during the detachment stage). An energy analysis of the bubble between plates during the residence stage was conducted, focusing primarily on the elastic potential energy (E_e) and surface energy (E_s) . As shown in Fig. 8(a), the residence time could be divided into two stages: the decelerated stage and the accelerated stage, based on the bubble's velocity along the y-axis. The moment when acceleration began, denoted as t_a , was marked with an empty triangle symbol. A clear deceleration period was observed for cases involving plates with low elastic modulus. Despite the identical input energy of the system, caused by the consistent liquid velocity from the inlet, the bubble surface energy (E_s) variation curve displayed distinct trends in Fig. 8(b). During the decelerated stage, the bubble surface energy in the elastic region exhibited a similar trend to the contact length (Δl), with a decreasing Δl leading to a reduction in E_s . The reduction in contact length (Δl) in the elastic region corresponded to the plates opening up, as seen in Fig. 5(b) and 5(c). The bubble elongated along the x-axis as the plate distance increased, thereby reducing the contact length for a constant bubble volume. Conversely, surface energy changes in the quasi-rigid region and rigid plates were minimal ($\Delta E_{\rm S}$ < 1.7×10^{-7} J) and nearly constant in rigid cases.

Fig. 8(c) shows that the release of bubble surface energy promoted an increase in elastic potential energy during the decelerated stage. In this stage, elastic potential energy continued to rise as the plates opened and increased more significantly in the elastic region. While it is generally understood that smaller elasticity leads to larger deflection for the same action, and that elastic potential energy depends on deflection magnitude, cases with the smallest elastic modulus ($E=2\times10^6$ Pa) did not show the highest increase in elastic potential energy. This inconsistency is likely influenced by the smaller deflection at the free end of the plate with low elastic modulus during the decelerated stage, as shown in Fig. 5

(b). As shown in Fig. 8(a), 8(b), and 8(c), the elastic potential energy (E_e) of the plate increased, while the bubble velocity (u_B) and surface energy (E_s) decreased before time t_a . After t_a , the elastic potential energy decreased, whereas the bubble velocity and surface energy increased rapidly. This indicates that the bubble's kinetic energy and surface energy were converted into the plate's elastic potential energy during the expansion phase of the plate. Subsequently, during the recovery phase, the plate's stored energy was transferred back to the bubble, significantly increasing its velocity. Fig. 8(d) illustrates the changes in total energy for both the bubble and the plate during the deceleration and acceleration stages. The total energy of the bubble (E_b) consists of its kinetic energy and surface energy, while the total energy of the plate (E_p) includes its elastic potential energy and kinetic energy. During the deceleration stage, the change in total energy of the bubble ($\Delta E_{\rm b}$) was negative, whereas the change in total energy of the plate (ΔE_p) was positive, indicating an energy transfer from the bubble to the plate. During the acceleration phase, a positive $\Delta E_{\rm b}$ and a negative $\Delta E_{\rm p}$ were observed in the elastic region, signifying an energy transfer from the plate to the bubble. Conversely, in the quasi-rigid region, $\Delta E_{\rm p}$ became positive while $\Delta E_{\rm h}$ turned negative, indicating that the plate continued to draw energy from the bubble. As depicted in Fig. 8(d), the energy released by the plate in the elastic region was significantly higher, and the case with $E = 7 \times 10^7$ Pa exhibited the largest increase in bubble energy.

The non-monotonic changes in contact length for cases with low elastic modulus emphasize the need to examine the plate morphology during the bubble departure process. The deflection of the plate with $E=2\times 10^6$ Pa was observed to be smaller than that of the plate highlighted in orange in Fig. 5(b) during the opening phase. For cases with the same bubble height, a smaller elastic modulus corresponded to larger plate displacement, which in turn reduced the contact length between the bubble and the plate. It is suggested that the flexible plates exhibited non-proportional morphology during the bubble residence stage. To characterize this changing morphology, the morphology factor ($\beta=y_x/y_{\rm tip}$) was introduced, where $y_{\rm tip}$ represents the y-coordinate of the free end of the flexible plate, and y_x is the y-coordinate at a specific x-coordinate. Taking the left plate as an example, the specific x-coordinate was selected as:

$$\mathbf{x} = \begin{cases} |\mathbf{x}|_{\text{max}} &, \left| \frac{\Delta \delta}{\Delta t} \right| > 0 \\ |\mathbf{x}|_{\text{min}} &, \left| \frac{\Delta \delta}{\Delta t} \right| \le 0 \end{cases}$$
 (16)

Where $\Delta\delta$ represents the change in deflection of the free end of the plate, and $|\Delta\delta/\Delta t|>0$ indicates the opening and closing processes of plates, the point of maximum absolute value of x on the plate boundary with the origin at the base of the left plate is selected as a special point at this time; and $|\Delta\delta/\Delta t|\leq 0$ indicates the recovery process of plates, the minimum absolute value |x|min was chosen as a special point. β would equal 1 if a pattern of trapezoid was formed by two plates during

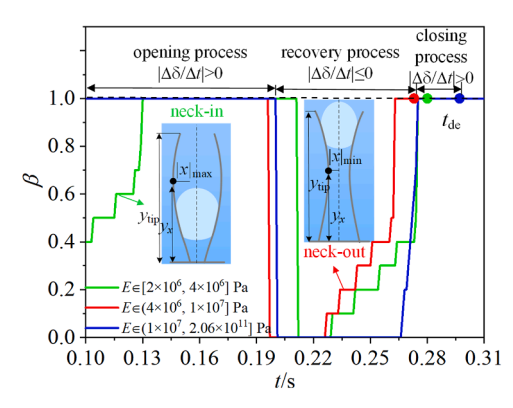


Fig. 9. Changes in plate morphology factors.

opening or closing processes, and it equaled to 0 during recovery process because |x|min was always located at the base of plates. However, it was found that β was not always equal 0 or 1 during the deflection process for cases with low elastic modulus ($E \leq 1 \times 10^7$ Pa) as shown in Fig. 9, which indicated that the plate was not always deflected along a straight line. From our observations on plate dynamics, it was found that a "necked-in" pattern formed by a pair of plates occurred in the range of $E \leq 4 \times 10^6$ Pa ($\beta < 1$) in the opening process, and the "necked-out" morphology appeared when $E \leq 1 \times 10^7$ Pa ($\beta < 1$) during the recovery process. it proved that the plate had the morphology of "necked-in "or "necked-out" if β took the value in the range of (0, 1) during the plate motion.

The "necked-in" morphology observed within the elastic region (2 imes $10^6 \le E \le 4 \times 10^6$ Pa) restricted the free end of the elastic plate from opening, causing plates with lower elasticity to exhibit smaller deflections under identical bubble forces (highlighted in the orange region of Fig. 5(b)). As previously explained, the opening of the elastic plate for a constant bubble volume stretched the bubble along the x-axis, reducing its contact length. As depicted in Fig. 5(b), the contact length for $E=2\times 10^6$ Pa was smaller than that for $E=7\times 10^6$ Pa. This indicated that, while the outward expansion of the plate with $E=2 \times$ 10° Pa was greater than that of $E = 7 \times 10^{\circ}$ Pa, its free-end deflection was smaller, producing a "necked-in" effect. This pattern hindered elastic potential energy storage during plate opening, slowing the rise of elastic potential energy (Ee), as shown by the green line in Fig. 8(c), and consequently extending the bubble's deceleration phase. During the recovery phase, the "necked-out" morphology accelerated the elastic plate's return motion, as observed in the orange box of Fig. 5(b). Elastic plates with low elastic modulus values ($E = 2 \times 10^6$ and 7×10^6 Pa) quickly returned to their original positions. Interestingly, the plate with $E = 7 \times 10^6$ Pa bypassed the "necked-in" morphology during opening, instead transitioning directly into a "necked-out" configuration during recovery. For "necked-out" morphologies, a surface tension imbalance arose between the bubble's top and bottom, leading to differences in Laplace pressure. This pressure gradient generated a net upward thrust that drove the bubble's ascent and detachment. These unique elastic plate deformations not only altered the forces acting on the bubble but also significantly affected elastic potential energy dynamics. The "necked-in" morphology restricted plate motion, reducing elastic potential energy and extending the bubble's deceleration stage. Conversely, the "necked-out" morphology facilitated rapid energy release during the recovery phase, enhancing the bubble's kinetic energy and promoting detachment. Elastic plates with higher elastic modulus values ($E=3\times10^7$ and 3×10^8 Pa) exhibited slower return movements, as shown in Fig. 5(b). This highlights that shortening the bubble detachment phase within the elastic region is critical to accelerating bubble separation. The energy released during this phase is closely tied to the elastic potential energy stored during both the plate opening and recovery processes.

The bubble dynamics between flexible plates indeed exhibited unique morphologies only at specific elastic modulus values. This phenomenon, involving the transition from a solid-liquid to a solid-gas interface during plate deformation, highlights the role of the elastic energy surpassing surface energy and viscous dissipation in triggering the "necked-in" morphology. The elastic capillary effect becomes particularly prominent when the elastic capillary length exceeds the diameter of the bubble or droplet. With the bubble's equivalent diameter being R=1.693 mm in this study, the critical elastic modulus for deformation was determined as follows [62]:

$$E = \frac{24\sigma R^2 (1 - \nu^2)(1 + \cos\theta_w)}{h^3}$$
 (17)

The critical elastic modulus is $E = 1.063 \times 10^7$ Pa in our case. It is important to highlight that the critical elastic modulus calculation did not account for liquid viscous dissipation, which means the actual elastic

modulus required for deformation would be slightly lower. In this study, the effective elastic modulus was determined to be 4×10^6 Pa, consistent with the theoretical findings. Based on this, it can be concluded that elastic plates with an elastic modulus slightly below the critical value are optimal for promoting bubble departure. In this case, the ideal value was found to be 7×10^6 Pa, which is notably less than the critical elastic modulus of 1.063×10^7 Pa.

4. Conclusions

Numerical investigations have explored bubble and plate dynamics within a confined elastic channel for the first time, uncovering critical insights. The study identified an optimal elasticity modulus that minimizes bubble departure time. Two distinct regimes—bubble residence and rapid bubble departure—were defined based on dynamic behavior. Energy transfer between bubble energy (kinetic and surface) and the elastic potential energy of the plates was closely analyzed. Key findings include:

- 1) Elastic modulus significantly influences bubble departure time. The optimal value which led to the shortest bubble motion period, 7×10^6 Pa, reduced bubble departure time by 10.2 % compared to rigid plates.
- 2) Coupled dynamics and energy conversion played a vital role. When a bubble departed, elastic potential energy not only transformed into the kinetic energy of plates and fluid, but also transformed into the bubble's kinetic energy, reducing bubble departure time. When $E=7\times 10^6$ Pa, elastic potential energy from the plates was converted more into bubble's kinetic energy than in the case of other elastic modulus, significantly reducing departure time.
- 3) Unique plate morphologies, such as necked-in and necked-out shapes, were observed for elastic plates with $E < 1 \times 10^7$ Pa. The necked-out shape aids bubble departure by storing more elastic potential energy.

These findings suggest a critical elastic modulus for designing elastic channels that enhance bubble departure efficiency. It is beneficial for boiling in confined space where bubble blockage is an annoying problem for these devices.

CRediT authorship contribution statement

Xiaojing Ma: Writing – original draft, Supervision, Conceptualization, Project administration. Songhe Wang: Investigation, Validation. ShiXin Nong: Data curation, Investigation. Chunjiao Han: Methodology, Validation. Jinliang Xu: Writing – review & editing. Khellil Sefiane: Writing – review & editing, Supervision.

Declaration of competing interest

All authors disclosed no relevant relationships.

Acknowledgements

This work was supported by the National Natural Science Foundation of China (No. 52206196) and the National Key R&D Program of China (No. 2023YFB4102400).

Data availability

Data will be made available on request.

References

- [1] F. Rocha, C. Georgiadis, K. Van Droogenbroek, Proton exchange membrane-like alkaline water electrolysis using flow-engineered three-dimensional electrodes, Nat. Commun. 15 (2024) 7444.
- L. Zhang, C. Wang, G. Su, A unifying criterion of the boiling crisis, Nat. Commun. 14 (2023) 2321.
- [3] M. Song, O.A. Sapozhnikov, V.A. Khokhlova, Dynamic mode decomposition based doppler monitoring of de novo cavitation induced by pulsed HIFU: an in vivo feasibility study, Sci. Rep. 14 (2024) 22295.
- [4] Y. He, Y. Cui, Z. Zhao, Strategies for bubble removal in electrochemical systems, Energy Rev. 2 (1) (2023) 100015.
- [5] R.A. Barmin, P.G. Rudakovskaya, O.I. Gusliakova, Air-filled bubbles stabilized by gold nanoparticle/photodynamic dye hybrid structures for theranostics, Nanomaterials 11 (2) (2021) 415.
- [6] G. Giustini, S. Jung, H. Kim, Evaporative thermal resistance and its influence on microscopic bubble growth, Int. J. Heat. Mass Transf. 101 (2016) 733-741.
- [7] B. Qi, J. Wei, X. Wang, Influences of wake-effects on bubble dynamics by utilizing micro-pin-finned surfaces under microgravity, Appl. Therm. Eng. 113 (2017) 1332-1344
- T. Ami, T. Schulenberg, Prediction of wetting phenomena of a microlayer of gas bubbles Int. J. Heat. Mass Transf. 133 (2019) 769-777.
- [9] A. Inbaoli, C.S. Sujith Kumar, S. Jayaraj, A review on techniques to alter the bubble dynamics in pool boiling, Appl. Therm. Eng. 214 (2022) 118805.
- [10] J. Bi, D.M. Christopher, D. Zhao, Numerical study of bubble growth and merger characteristics during nucleate boiling, Prog. Nucl. Energy 112 (2019) 7–19.
- [11] S.T. Kadam, I. Hassan, R. Kumar, Bubble dynamics in microchannel; an overview of the state-of-the-art, Meccanica 56 (2021) 481-513.
- [12] M. Hatipogullari, C. Wylock, M. Pradas, Contact angle hysteresis in a microchannel: statics, Phys. Rev. Fluids. 4 (4) (2019) 044008.
- [13] S.G. Kandlikar, A scale analysis based theoretical force balance model for critical heat flux (CHF) during saturated flow boiling in microchannels and minichannels. 2010, 132(8): 081501.
- S.G. Kandlikar, Evaporation momentum force and its relevance to boiling heat transfer, J. Heat Transf. 142 (10) (2020) 100801.
- Y. Guo, G. Wang, D. Qian, Accident safety analysis of flow blockage in an assembly in the JRR-3M research reactor using system code RELAP5 and CFD code FLUENT, Ann. Nucl. Energy 122 (2018) 125-136.
- [16] R. Xu, X. Xu, M. He, Controllable manipulation of bubbles in water by using underwater superaerophobic graphene-oxide/gold-nanoparticle composite surfaces, Nanoscale 10 (1) (2018) 231-238.
- [17] A.A. Ala, S. Tan, S. Qiao, Simulation of the effect of partial and total blockage of a sub-channel on two-phase flow through a 5×5 square rod bundle, Prog. Nucl. Energy 155 (2023) 104514.
- [18] L. Pan, R. Yan, H. Huang, Experimental study on the flow boiling pressure drop characteristics in parallel multiple microchannels, Int. J. Heat. Mass Transf. 116 (2018) 642-654
- [19] G.F. Swiegers, R.N.L. Terrett, G. Tsekouras, The prospects of developing a highly energy-efficient water electrolyser by eliminating or mitigating bubble effects, Sustain. Energy Fuels. 5 (5) (2021) 1280-1310.
- A.E. Bergles, ExHFT for fourth generation heat transfer technology, Exp. Therm. Fluid. Sci. 26 (2-4) (2002) 335-344.
- M.H. Mousa, C.M. Yang, K. Nawaz, Review of heat transfer enhancement techniques in two-phase flows for highly efficient and sustainable cooling, Renew. Sustain. Energy Rev. 155 (2022) 111896.
- [22] K. Fei, W.H. Chen, C.W. Hong, Microfluidic analysis of CO₂ bubble dynamics using thermal lattice-boltzmann method, Microfluid. Nanofluidics. 5 (2008) 119-129.
- [23] G. Okech, M. Emam, S. Mori, Experimental study on the effect of new anode flow field designs on the performance of direct methanol fuel cells, Energy Convers. Manage 301 (2024) 117988.
- E. Turkoz, J. Brandman, D. Ertas, Understanding diffusion-controlled bubble growth in porous media using experiments and simulations, Phys. Rev. E 108 (1) 2023) 015105.
- [25] G.D. Xia, Y.X. Tang, L.X. Zong, Experimental investigation of flow boiling characteristics in microchannels with the sinusoidal wavy sidewall, Int. Commun. Heat Mass Transf. 101 (2019) 89-102.
- [26] M.K. Gupta, D.S. Sharma, V.J. Lakhera, Vapor bubble formation, forces, and induced vibration: a review, Appl. Mech. Rev. 68 (3) (2016) 030801.
- H. Liu, Q. Lu, L. Pan, A modified force balance model for predicting bubble departure diameter and lift-off diameter in subcooled flow boiling, Int. J. Heat. Mass Transf. 221 (2024) 125058.
- [28] J.F. Klausner, R. Mei, D.M. Bernhard, Vapor bubble departure in forced convection boiling, Int. J. Heat. Mass Transf. 36 (3) (1993) 651–662.
- X. Yang, D. Baczyzmalski, C. Cierpka, Marangoni convection at electrogenerated hydrogen bubbles, Phys. Chem. Chem. Phys. 20 (17) (2018) 11542-11548.

- [30] P. Kangude, A. Srivastava, Understanding the growth mechanism of single vapor bubble on a hydrophobic surface: experiments under nucleate pool boiling regime, Int. J. Heat. Mass Transf. 154 (2020) 119775.
- [31] W. Gao, J. Qi, X. Yang, Experimental investigation on bubble departure diameter in pool boiling under sub-atmospheric pressure, Int. J. Heat. Mass Transf. 134 (2019) 933-947.
- M. Lebon, J. Sebilleau, C. Colin, Dynamics of growth and detachment of an isolated bubble on an inclined surface, Phys. Rev. Fluids. 3 (7) (2018) 073602.
- [33] A. Angulo, P. Van. Der. Linde, H. Gardeniers, Influence of bubbles on the energy conversion efficiency of electrochemical reactors, Joule 4 (3) (2020) 555-579.
- J. Wang, Y. Zheng, F.Q. Nie, Air bubble bursting effect of lotus leaf, Int. Conf. Micro-Nanoscale Heat Transf. 43901 (2009) 667-674.
- [35] D. Guo S, X.B. Li, H.N. Zhang, Bubble behaviors during subcooled pool boiling in water and nonionic surfactant aqueous solution, Int. J. Heat. Mass Transf. 159 (2020) 120087.
- [36] X. Lu, T. Nie, X. Li, Insight into pH-controlled bubble dynamics on a Pt electrode during electrochemical water splitting, Phys. Fluids 35 (10) (2023).
- [37] P. Hadikhani, S.M.H. Hashemi, D. Psaltis, The impact of surfactants on the inertial separation of bubbles in microfluidic electrolyzers, J. Electrochem. Soc. 167 (13) (2020) 134504.
- [38] M. Rastello, J.L. Marié, M. Lance, Clean versus contaminated bubbles in a solidbody rotating flow, J. Fluid. Mech. 831 (2017) 592-617.
- G. Hetsroni, A. Mosyak, E. Pogrebnyak, Effect of Marangoni flow on subcooled pool boiling on micro-scale and macro-scale heaters in water and surfactant solutions, Int. J. Heat. Mass Transf. 89 (2015) 425-432.
- [40] L. Xu, J. Xu, Nanofluid stabilizes and enhances convective boiling heat transfer in a single microchannel, Int. J. Heat. Mass Transf. 55 (21-22) (2012) 5673-5686.
- L. Yu, A. Sur, D. Liu, Flow boiling heat transfer and two-phase flow instability of nanofluids in a minichannel, J. Heat Transf. 137 (5) (2015) 051502.
- [42] N. Mao, J. Zhuang, T. He, A critical review on measures to suppress flow boiling instabilities in microchannels, Heat. Mass Transf. 57 (6) (2021) 889-910.
- [43] L. Yin, K. Zhang, T. Qin, Boiling bubble behaviors of fluids of different surface tensions on heating surfaces with micro-nanostructures, Phys. Fluids 37 (1) (2025).
- [44] N. Laskar, M.K. Das, Unveiling the underlying physics of two-phase boiling heat transfer enhancement through shearing of coalescing bubbles, Phys. Fluids 36 (9) (2024).
- J. Camarasa, M. Vilarrubí, M. Ibáñez, Experimental study of flow boiling cooling in a novel variable density pin-fin device, Appl. Therm. Eng. 269 (2025) 126023.
- [46] D.D. Meng, Micro-pumping of liquid by directional growth and selective venting of gas bubbles, Lab. Chip. 8 (6) (2008) 958-968.
- P.C. Lee, F.G. Tseng, C. Pan, Bubble dynamics in microchannels. Part I: single microchannel, Int. J. Heat. Mass Transf. 47 (2004) 5575.
- C. Yu, Z. Xu, S. He, Tian, L. Jiang, Manipulating boiling bubble dynamics on underliquid superaerophobic silicon surfaces for high-performance phase-change cooling, Adv. Funct. Mater. 35 (2025) 2420677.
- [49] Y. Sun, Z. Zhang, G. Zhang, Effect of surface wettability on bubble dynamics and heat transfer in microchannel flow boiling, Int. J. Heat. Mass Transf. 241 (2025) 126729.
- [50] C. Zhang, X. Xiao, Y. Zhang, Bioinspired anisotropic slippery cilia for stiffnesscontrollable bubble transport, ACS. Nano 16 (6) (2022) 9348-9358.
- C.J. Han, M. He, X.J. Ma, Bubble necking in a confined channel formed by a pair of elastic plates, Int. J. Heat. Fluid. Flow. 107 (2024) 109425.
- X.J. Ma, M. He, C.J. Han, Boiling heat transfer enhancement by a pair of elastic plates, Int. J. Heat. Mass Transf. 227 (2024) 125580.
- G.F. Wu, Numerical and Experimental Study On Interaction Between Underwater Explosion Bubble On Flexible Structure, Harbin Engineering University, 2020.
- G. Lin, J.M. Frostad, G.G. Fuller, Influence of interfacial elasticity on liquid
- entrainment in thin foam films, Phys. Rev. Fluids. 3 (11) (2018) 114001. T. Tofan, H. Kruggel-Emden, V. Turla, R. Jasevičius, Numerical modeling of the motion and interaction of a droplet of an inkjet printing process with a flat surface, Appl. Sci. 11 (2021) 527.
- [56] J. Shen, X. Yang, Energy stable schemes for Cahn-Hilliard phase-field model of twophase incompressible flows, Chin. Ann. Math. B 31 (2010) 743.
- P. Yue, J. Feng, C. Liu, J. Shen, A diffuse-interface method of simulating two-phase flows of complex fluids, J. Fluid. Mech. 515 (2004) 293.
- [58] X. Zhou, Y. Xu, Q. Zhang, W. Zhang, Droplet impact on a flexible disk, J. Fluid. Mech. 1002 (2025) A8.
- R. Krishna, J.M. Van. Baten, Mass transfer in bubble columns, Catal. Today 79 (2003) 67-75.
- T. Madhavi, A.K. Golder, A.N. Samanta, Studies on bubble dynamics with mass transfer, Chem. Eng. J. 128 (2-3) (2007) 95-104.
- Y. Ma, H. Huang, Scaling maximum spreading of droplet impacting on flexible substrates, J. Fluid. Mech. 958 (2023) A35.
- Y.P. Zhao, Physical Mechanics on the Surface and Interface, Science Press, Beijing, 2012.